Electrochemical sensors onboard a Zeppelin NT: In-flight evaluation of low-cost trace gas measurements

Tobias Schuldt[1], Georgios I. Gkatzelis[1], Christian Wesolek[1], Franz Rohrer[1], Benjamin Winter[1], Thomas A. J. Kuhlbusch[2], Astrid Kiendler-Scharr[1], Ralf Tillmann[1]

5   [1]Institute of Energy and Climate Research, IEK-8: Troposphere, Forschungszentrum Jülich GmbH, Jülich, Germany
[2]Federal Institute for Occupational Safety and Health (BAuA), Dortmund, Germany

Correspondence to: Tobias Schuldt (t.schuldt@fz.juelich.de), Georgios I. Gkatzelis (g.gkatzelis@fz-juelich.de)

Abstract

In this work we used a Zeppelin NT equipped with six sensor setups, each composed of four different low-cost electrochemical
10   sensors (ECS) to measure nitrogen oxides (NO and NO_2), carbon monoxide, and Ox (NO_2 + O_3) in Germany. Additionally, a MIRO MGA laser absorption spectrometer was installed as a reference device for in-flight evaluation of the ECS. We report the influence of temperature on the NO and NO_2 sensor outputs, but also find a shorter time scale (1 s) dependence of the sensors on the relative humidity gradient. To account for these dependencies, we developed a correction method that is independent of the reference instrument. After applying this correction to all individual sensors, we compare the sensor setups
15   with each other and to the reference device. For the intercomparison of all six setups we find good agreements with $R^2 \geq 0.8$, but different precisions for each sensor in the range of 1.45 to 6.32 ppb. The comparison to the reference device results in an R^2 of 0.88 and a slope of 0.92 for NO_x (NO + NO_2). Furthermore, the average noise (1 σ) of the NO and NO_2 sensors reduces significantly from 6.25 ppb and 7.1 ppb to 1.95 ppb and 3.32 ppb, respectively. Finally, we highlight the potential use of ECS in airborne applications, by identifying different pollution sources related to industrial and traffic emissions during multiple
20   commercial and targeted Zeppelin flights in spring 2020. These results are a first milestone towards the quality-assured use of low-cost sensors in airborne settings without a reference device, e.g., on unmanned aerial vehicles (UAVs).

Keywords

Sensor, low cost, airborne, air pollution, trace gas

25   **1 Introduction**

The effects of poor air quality are manifold – they are environmental (e.g., Mclaughlin, 1985; Bytnerowicz et al., 2007), economic (e.g., Quah and Boon, 2003), and health-related (e.g., Kampa and Castanas, 2008; Von Schneidemesser et al., 2020). Ambient air quality is dependent on the level of pollutant concentrations in the lower troposphere that includes both airborne particles and gaseous substances. Increasing concentrations of target pollutants, i.e., particulate matter, PM, nitrogen dioxide
30   (NO_2), and ozone (O_3) increase the risk of cardiovascular, respiratory, and cerebrovascular mortality for short-term (Orellano

et al., 2020) as well as long-term exposure (Huangfu and Atkinson, 2020; Chen and Hoek, 2020). Furthermore, these pollutants can influence climate change with either cooling or warming effects (IPCC, 2021). Historically, in order to limit such impacts the World Health Organization (WHO, 2021) and the Intergovernmental Panel for Climate Change (IPCC, 2021) set global guidelines for countries to achieve. Quantification of pollutants is, therefore, an essential procedure for assessing air quality

35 and climate change and the first step through which subsequent action can be taken.

In Europe, this has been largely achieved via ground-based monitoring networks, such as the European Environment Agency's European Monitoring and Evaluation Programme (EMEP; http://ebas.nilu.no), or even infrastructures such as the Aerosols, Clouds, and Trace Gases Research Infrastructure (ACTRIS; https://www.actris.eu), that provide high-quality data for criteria pollutant concentrations around the world. The EU Air Quality Directive 2008/50/EC with its amendment 2015/1480/EC was

40 introduced to create uniform requirements for air quality measurements. In Germany, the measuring stations are operated by the State Environmental Agencies and the Federal Environment Agency in accordance with the Air Quality Directive's specifications. However, such ground-based measurements are typically stationary and thus cover local air quality trends with limited insights on the vertical distribution of pollutants or small-scale spatial gradients (Apte et al., 2017; Messier et al., 2018). Furthermore, maintenance and operation of such networks at the spatial resolution needed to inform decision makers, may

45 exceed available budgets.

In the last years, development of *low-cost sensors* e.g., electrochemical sensors (ECS), whose costs are two to three orders of magnitude lower than those of typical laboratory-grade devices, have been used as an alternative and affordable option to perform measurements that cover multiple locations (Popoola et al., 2018; Rai et al., 2017; Shusterman et al., 2016; Sun et al., 2016; Mead et al., 2013). Such sensors have been extensively used and evaluated alongside measuring stations (Popoola et al.,

50 2018; Sahu et al., 2021; Mead et al., 2013; Dallo et al., 2021; Spinelle et al., 2017, 2015) and have recently been extended for airborne applications (Villa et al., 2016; Schuyler and Guzman, 2017; Gu et al., 2018; Mawrence et al., 2020; Pochwala et al., 2020; Pang et al., 2021; Bretschneider et al., 2022). ECSs are light, compact in size, and of low power consumption (Alphasense, 2019b, a, f, e, d) - properties required for use on unmanned aerial vehicles (UAV); however, evaluation compared to reference devices in such airborne applications still remains a challenge.

55 Data quality assurance of ECSs is an essential step due to their cross-sensitivities to a wide range of influencing factors. These include meteorological parameters such as temperature (Mead et al., 2013; Popoola et al., 2016) and relative humidity (Samad et al., 2020; Wei et al., 2018), as well as cross-sensitivities to other gases (Mueller et al., 2017; Pang et al., 2018; Lewis et al., 2016). Furthermore, the gradients of meteorological parameters like the rate of relative humidity changes (% s^{-1}) can influence the sensor signal with slow recovery times of up to hours (Mueller et al., 2017; Pang et al., 2018; Pang et al., 2017). There are

60 two possible scenarios to compensate for such interferences: hardware modifications and post-processing of the data. Examples for hardware modifications are the introduction of a fourth electrode in the typical three-electrode electrochemical sensor to compensate for zero shifts (Baron and Saffell, 2017) and the implementation of a filter for specific cross interfering gases, e. g. for O_3 in an NO_2 ECS (Hossain et al., 2016). On the post-processing side, a growing variety of methods are used to obtain sufficient data quality. These include parametric algorithms such as multiple linear regressions (Wei et al., 2018), but also non-

65 parametric methods such as decision trees (Zimmerman et al., 2018), artificial neural networks (Han et al., 2021) or other numerical models (Cross et al., 2017). M*achine learning* is often used as an equivalent term for non-parametric models (WMO, 2018). It has the advantage to identify more complex interferences in large datasets, such as non-linearities, time dependencies, or combined interferences. A limitation, however, is that the cause of these interferences remains unknown when using machine learning models, in contrast to e.g., linear regression methods where such dependencies can be identified.

70 In this work, we evaluate the performance of low-cost sensors and develop a correction method that accounts for ECS interferences based on real-time airborne observations onboard a Zeppelin NT. This includes the measurements of CO, NO, NO_2 and Ox ($NO_2 + O_3$) that are compared to the MIRO MGA (Tillmann et al., 2022) used as a reference device to evaluate the performance of the sensors. We show that ECSs can be used for reliable, in situ trace gas measurements and highlight their potential for airborne applications aboard UAVs.

2 Methods

2.1 Experimental setup / platform
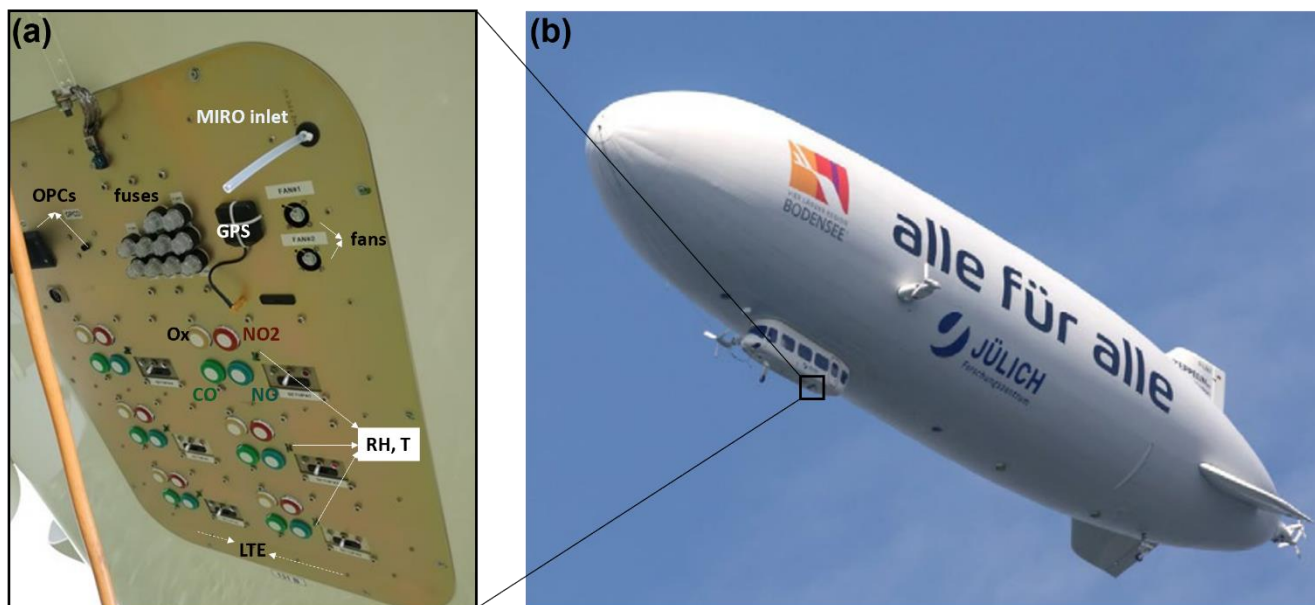
Figure 1: (a) Hatch box including the sensor setups located on the bottom of the (b) Zeppelin NT (© Forschungszentrum Jülich / Ralf-Uwe Limbach) that was used as the measurement platform in this work. The reference device, MIRO MGA, was installed
80 **inside the gondola, but with the inlet line right beside the sensor setups, shown in the top right of panel (a).**

Figure 1 shows the experimental setup for the in situ airborne measurements. This includes a Zeppelin NT (b) as a measurement platform equipped with a hatch box (a), located on the bottom of the airship. The Zeppelin NT is particularly suitable for planetary boundary layer (PBL) measurements due to its long flight duration (up to 20 h) at low altitudes below 1 km, a high

payload of around 1000 kg, and good manoeuvrability. This allows measurements within the PBL to investigate the influence

85   of different urban emission sources on air quality (Tillmann et al., 2022).

Six electrochemical sensor (ECS) setups are installed at the hatch box, together with a GPS module (Adafruit Ultimate GPS), Long Term Evolution (LTE) – a standard for wireless broadband communication for mobile devices – equipment for remote access, ventilation fans to regulate the hatch box pressure, two optical particle counters, and fuses to protect the electronics. The hatch box dimensions are 738×538×162 (length × width × height in mm). The sensor inlets are located outside of the

90   hatch box and exposed to ambient air via diffusion. A sensor setup, as shown in Fig S1, consists of four ECS to measure the trace gases CO, NO, NO_2 and Ox ($NO_2 + O_3$), a Telaire ChipCap 2 sensor for temperature and relative humidity measurements and a self-developed printed circuit board (PCB) for managing and saving the incoming data with a frequency of 1 Hz. Further specifications of the sensors are given in Table 1. The setups are powered from the Zeppelin NT and further supported by two batteries to provide uninterrupted power to the sensors.

95

Table 1: Specifications of each sensor setup.

Parameter	Sensor	Principle	Response time[a]	Accuracy[a]	Range[a]
CO	Alphasense CO-B4	Amperometric	< 30 s (t_{90})	±4 ppb (precision, 2σ)	0-1000 ppm
NO	Alphasense NO-B4	Amperometric	< 45 s (t_{90})	±15 ppb (precision, 2σ)	0-20 ppm
NO_2	Alphasense NO2-B43F	Amperometric	< 80 s (t_{90})	±15 ppb (precision, 2σ)	0-20 ppm
Ox ($NO_2 + O_3$)	Alphasense Ox-B431	Amperometric	< 80 s (t_{90})	±15 ppb (precision, 2σ)	0-20 ppm
Aerosol (Size distribution, PM_1, $PM_{2.5}$, PM_{10})[b]	Alphasense OPC-N3	Light scattering	1-30 s (sampling interval)	-	0.35 - 40 µm
Temperature		CMOS	5 s (t_{63})	±0.3 °C	-40 to 125 °C
Relative Humidity	Telaire ChipCap 2	Capacitive	4 s (t_{63})	±2.0 % RH (20-80 % RH)	0 - 100 % RH (Non-Condensing)

[a] Specifications given in the corresponding data sheets.
[b] Connected to setup #1 and #4 but not used in this work.

100   In this study we focus on the measurements of NO and NO_2 (NO_x) using electrochemical sensors from Alphasense (UK, Essex). Laboratory evaluation and optimization of the CO and O_x sensor performance is currently ongoing, and the focus of a future study as further discussed in section 2.3.3. Here, the NO_x measurements are performed using amperometric gas sensors that have four electrodes: a *working electrode* (*WE*), a *counter electrode* (*CE*), a *reference electrode* (*RE*), and the *auxiliary electrode* (*AUX*). The measuring principle is based on a redox reaction that takes place at the *WE* and the *CE* (reduction,

105   oxidation). The *RE* keeps the *WE* at a constant potential to force the desired electrochemical reaction of the analyte on the three-phase boundary (electrode, electrolyte, gas). The resulting charges are transferred to each electrode in the form of ions

via the electrolyte solution and in the form of electrons via an external circuit. The resulting current of the electron transfer is the measurement signal of the sensor. This current is exactly proportional to the concentration of the analyte when the sensor is operated under appropriate diffusion-limited conditions. Many kinetic factors, such as the mass transfer of the analyte to the

110   electrode as well as the electrocatalytic activity of the electrode material, can be adjusted via the design of the sensor (Stetter and Li, 2008). *AUX* has the same design as the *WE*, but is fully immersed in the electrolyte and has no interface with the gas phase (Baron and Saffell, 2017). Therefore, the *AUX* signal can be used to correct the *WE* signal from influences on the *WE* other than the analyte (e.g., temperature). The measured *WE* and *AUX* currents are converted into a voltage signal using an individual sensor board (ISB, Alphasense). Finally, this signal is digitised by the measurement board and then recorded on an

115   SD card in binary format and can also be transferred serially.

Besides the measurement equipment in the hatch box, a MIRO MGA10-GP multi-compound gas analyzer was installed in the gondola. The MIRO MGA measures the amount fractions of ten trace gases (NO, NO_2, O_3, SO_2, CO, CO_2, CH_4, H_2O, NH_3, N_2O) by direct laser absorption spectroscopy. In this study it is used as a reference system for the ECS and enables a direct performance evaluation of the ECS in an airborne setting. Hundt et al. (2018) and Liu et al. (2018) provide more in-depth

120   details about the MIRO, while more information on its use on the Zeppelin NT are given by Tillmann et al. (2022). For an accurate intercomparison to the ECSs, a perfluoroalkoxy alkane (PFA) inlet line with a length of 8 m was placed next to the ECSs in the hatch box (Fig. 1 (a)) and connected to the MIRO. The volumetric flowrate used for the MIRO was 1.2 SLM resulting in a residence time of the gas inside the line of around 5 s.
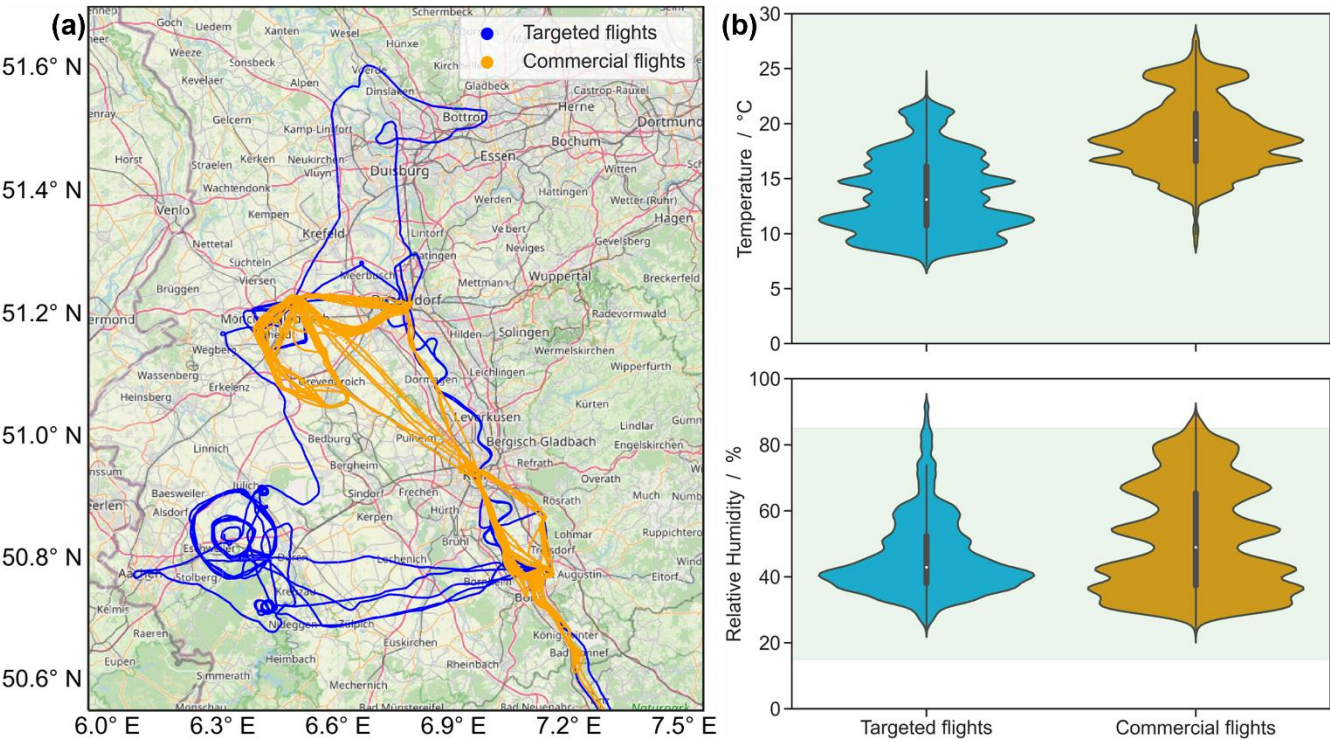
Figure 2: (a) Map with flight paths in North Rhine-Westphalia, Germany (© OpenStreetMap contributors 2021. Distributed under the Open Data Commons Open Database License (ODbL) v1.0), and (b) frequency distribution of the corresponding temperature and relative humidity in-flight values for the targeted (blue) and commercial (orange) flights - illustrated in violin plots. The manufacturer-specified limits within which the sensors should be used are depicted in shaded green in the background.

Figure 2 (a) depicts a map with the flight paths for our measurements in 2020. The flights took place within two periods in mid to late spring, with targeted research flights performed from 29 April 2020 to 09 May 2020 and measurements during commercial flights from 27 May 2020 to 15 June 2020. All flights were over Germany, and predominantly over North Rhine-Westphalia except for the transfer flights on 29 April 2020 and 27 May 2020 from Friedrichshafen to North Rhine-Westphalia, and from North Rhine-Westphalia back to Friedrichshafen on 09 May 2020 and 15 June 2020. During the targeted flights, specific emission sources e.g., a power plant were targeted as well as cities and rural areas. More detailed information on individual flights is provided by Tillmann et al. (2022). Figure 2 (b) shows the in-flight measured temperature and relative humidity values. According to the manufacturers specifications the sensors should be used in the range from -30 °C to 40 °C and 15 % to 85 % relative humidity (Alphasense, 2019b, a, e, d). Nearly the entire data set is within these specifications with 1 % and 99 % percentiles at 8.4 °C (1 %), 25.7 °C (99 %) and 28.0 % RH (1 %), 84.0 % RH (99 %), respectively. Furthermore, the manufacturer recommendations are given for continuous exposure at high or low RH which was not observed for the whole dataset hence limiting the influence of such interferences for this study.

2.3 Data processing

The quality of sensor data can be influenced by various parameters including transmission errors to the measurement board and electromagnetic interference between the devices (Alphasense, 2013), as well as defective sensor components. In this work, we use multiple ECS sensors in parallel to track defective sensors after following the steps that are outlined below.

2.3.1 Time synchronization and noise reduction

The clocks on each of the six sensor setups were manually pre-set, therefore time synchronization was not ensured. In the first step we chose a *master setup*, here setup #2 that was operational throughout all flights with a data coverage of 99 %. Next, a time shift was applied to the other setups to match it. To find the optimal values for this time shift, setup X was shifted from -60 s to +60 s stepwise by 1 s, performing a linear regression analysis (setup X(t+-x) vs. setup #2). The linear regression resulting in the highest coefficient of determination, R^2, was used to correct for the time difference of each setup to the master setup. This was done using the full dataset of each period of flights, targeted and commercial, resulting in shifts within ±15 s and an average time drift of ±0.31 s week^{-1}, leading to a maximum drift of $< \pm 1$ s during each single period of flights.

In the next step the data of the sensors and the MIRO MGA whose clock is set via LTE were synchronized. This synchronization step made it possible to properly compare the sensors with each other and with the reference instrument. Lastly, to reduce the noise of the ECS signals, a Savitzky-Golay filter (Savitzky and Golay, 1964) was used. Here, a polynomial regression with a window size of 2 n + 1 adjacent data points is solved by linear least squares. A window of 11 s (n = 5) and a polynomial degree of 3 was found to be optimal to smooth the signals without altering the analyte peaks. Fig. S3 shows the difference between the sensor signal before and after applying the filter at different NO and NO_2 concentrations. The signal reduction is within 10 ppb (2 σ, corresponding to around 95 % of the data), i.e., similar to the noise levels of the sensors (Fig. S2), independent of the NO and NO_2 concentrations, which highlights the minor influence of the Savitzky-Golay filter at larger peaks.

2.3.2 Temperature and relative humidity data

In addition, six ChipCap 2 sensors were used for temperature and relative humidity measurements. The sensors measurement principle is based on a capacity change for relative humidity and a resistance variation for temperature. To evaluate the performance of these sensors, we intercompared the differences between the six sensors as shown in Fig. S4. From these results it is evident that the temperature and relative humidity sensors of setups #4, #6 and partly #5 provide erroneous data. We therefore calculate and use throughout this work the mean values and standard deviations of the remaining, quality-assured temperature and relative humidity measurements, assuming response times within 5 s as shown in Table 1.

2.3.3 Determination of amount fractions

In this work, we develop a correction method to accurately determine the amount fractions of NO and NO_2 using regression parameters determined with the ECS in-flight data (Sect. 3). A detailed description of the correction procedure is given in the supplement and is based on the method of Mead et al. (2013). After applying this correction method, the sensor voltage signals in mV are converted to amount fractions using sensitivity values in mV/ppb provided by the manufacturer (Table S1). Here, we assume constant sensitivities given that their dependency, e.g., to temperature, is a 2nd order effect (Mead et al., 2013; Popoola et al., 2016).

To account for sensor response times, a low pass filter, in this case a centred moving average with a window size of 31 seconds is used that corresponds to the t_{90}, defined as the duration the sensor needs to reach 90 % of the final signal after a step change in concentration. This value is derived from the combined information given by the laboratory measurements (Table S2), in agreement with the manufacturer and published measurements (Mead et al., 2013): the manufacturer provides a t_{90} of < 45 s for NO and < 80 s for NO_2 from 0 to 2 ppm, whereas Mead et al. provide a t_{90} of 21 s for NO_2.

As a reference correction method, we use the recommended correction described by the manufacturer (Alphasense, 2019c) following the above equations to correct the NO and NO_2 *WE* output for effects of temperature:

$$WE_{NO,c} = (WE_u - WE_e) - k_T \times \left(\frac{WE_0}{AUX_0}\right) \times (AUX_u - AUX_e), \tag{1}$$

$$WE_{NO_2,c} = (WE_u - WE_e) - n_T \times (AUX_u - AUX_e), \tag{2}$$

where *WE* and *AUX* are the working and auxiliary electrode voltages. The subscripts u, e and 0 stand for the uncorrected, i.e., measured signal, the electronic offset, and the sensor zero, respectively. The electronic offsets and sensor zero values are provided by the manufacturer and given in Table S1. $WE_{NO,c}$ and $WE_{NO2,c}$ are the corrected working electrode voltages for NO and NO_2, respectively. The temperature compensation factors k_T and n_T are given in the range of -30 °C to 50 °C in 10 °C steps. For temperatures within these 10 °C steps, a linear interpolation is advised.

ECSs were also used to measure CO and Ox ($NO_2 + O_3$). A comparison of the ECS measurements to the MIRO reference instrument was performed after following the manufacturers recommendations to estimate amount fractions for CO and Ox. However, high uncertainties were found due to the high CO and O_3 backgrounds creating an offset to the sensors that was not accurately accounted for based on the manufacturer's correction procedure (Fig. S5). Additionally, the described correction procedure in the supplement used in this work for NO and NO_2 relies on periods with low analyte concentrations, ideally zero, to account for offsets of the background signal. While this is a good approximation for NO and NO_2 it is not applicable to CO and O_3 because of their higher background concentrations often above several tens of ppb. Laboratory evaluation and optimization of the CO and Ox sensor performance is currently ongoing and the focus of a future study. In this work we evaluate the performance and highlight the potential of the NO and NO_2 sensors for accurate airborne applications.

3 Results and discussion

3.1 Sensor signal dependencies

All Zeppelin measurements were filtered for periods of low NO and NO_2 concentrations ($<$ 2 ppb) using the measurement data of the reference instrument in order to find possible interferences on the *WE* signal of the electrochemical sensors. This procedure reduces the data to only background concentration periods and provides the signal that is influenced by cross interferences. The correction method developed and described in the following is entirely independent of a reference device and requires only the sensors used. Figure 3 and Figure S6 show the correlation of *WE* to *AUX*, *T*, and d*RH*/d*t* at different time resolutions (i.e., averaging intervals) for NO and NO_2, respectively. For 1 s resolution, coefficients of determination (R^2) are 0.86, 0.71, 0.83 for NO and 0.57, 0.13, 0.86 for NO_2, for *AUX*, *T*, and d*RH*/d*t*, respectively. For this data set, we could not detect any other significant dependencies including d*T*/d*t* (Fig. S7). As described in Sect. 2.1 *AUX* can be used to correct the *WE* signal from external interferences. The collinearity between *AUX* and *T*, that is shown by the colored dataset in Fig. 3 further promotes the significant influence of temperature on the sensor measurements. However, other unknown interferences could have a simultaneous effect on *WE* and *AUX*, such as changes of the electrolyte composition or influences on the sensor boards electronics that control the voltages of the electrodes. Therefore, we also consider *AUX* as an additional correction parameter despite the observed collinearity with temperature.
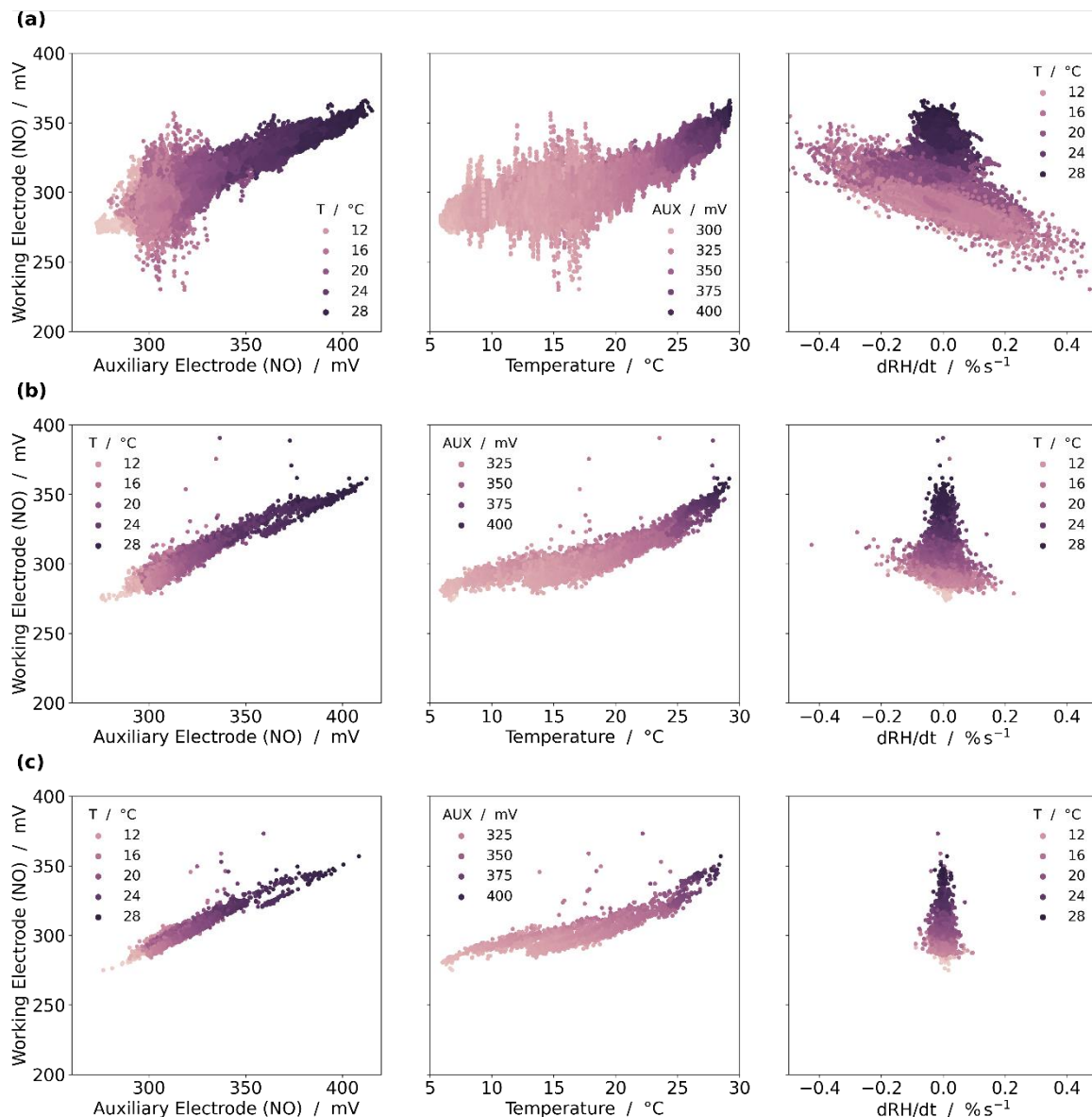
Figure 3: Scatterplots of NO sensor (setup #2) for *WE* vs. *AUX*, *T* and d*RH*/d*t* with different time resolutions of (a) 1 s, (b) 30 s and (c) 120 s provided per row. The colors are used to show collinearity between *AUX* and *T*, and that the shift of WE voltages in the d*RH*/d*t* plot is a temperature interference.

Figure 3 shows that temperature and *AUX* dependencies are effective on a longer timescale since the relationship with *WE* does not change with lower time resolutions transitioning from 1 s to 30 s and 120 s. On the contrary, the correlation with d*RH*/d*t* decreases progressively with decreasing time resolution. Since ECS are mostly deployed for long-term monitoring of air quality at e.g., stationary monitoring stations, mean values of up to 1 hour are often used (Mijling et al., 2018). Therefore, at longer time resolutions such effects are filtered out. However, for mobile applications, a high time resolution results in a better spatial resolution of the pollutant distributions, making this effect relevant.

Previous publications have shown the influence of humidity changes on the *WE* signal, after which there is a spike in the signal followed by a slow decay (Mueller et al., 2017; Pang et al., 2018; Pang et al., 2017). Mueller et al. (2017) conducted laboratory

230   tests with relative humidity changes of 5 % RH every 20 minutes between 40 % RH and 60 % RH. They observed that this changed the sensor signal by a similar order of magnitude as the addition of 70 ppb NO_2. Afterwards, the signal decreased exponentially in time back to equilibrium. Through further measurements, they found that the effect was dependent on the magnitude and rate of the relative humidity variation that can affect the measurement accuracy over minutes to hours – but the physical reason for this is currently unknown. Pang et al. (2017) came to a similar conclusion. Rapid RH changes (≈ 20 %/min)

235   had an immediate influence on the sensor signal followed by a required recovery period of up to 40 min to restore the original value whereas small humidity changes of about 0.1 %/min had no significant effect. When compared to our measurements, the humidity changes in these laboratory experiments are unidirectional and over a longer time scale. During the flights, we observe both negative and positive humidity changes on a short time scale. For example, the mentioned 20%/min *RH* change that triggers the long recovery phase results in 0.33 %/s, assuming a linear increase. During the Zeppelin flights we observe

240   such a longer lasting effect starting at about 0.7 %/s, after which it takes up to 5 min, for the signal to stabilise again, depending on the magnitude of the rate of change. Since we do not have an exact analytical solution for correcting this dependency yet, these values were removed from the data set. However, we were able to describe the dependence of the *WE* voltages to the temporally small-scale changes in relative humidity (max. ± 0.6 %/s), which affect the signals only immediately and briefly, with a linear relationship (see Fig. 3).

245   In the following, we use the above correlations on temperature, *AUX*, and d*RH*/d*t* to develop a correction method using the equations below for NO and NO_2.

$$WE_{NO,c}(t) = WE_{NO,a}(t) - \beta_0 \times \frac{dRH}{dt}(t) - (\alpha + \beta_1 \times \exp(\beta_2 \times T(t)) + \beta_3 \times AUX(t)), \tag{3}$$

$$WE_{NO_2,c}(t) = WE_{NO_2,a}(t) - \beta_0 \times \frac{dRH}{dt}(t) - (\alpha + \beta_1 \times T(t) + \beta_2 \times AUX(t)), \tag{4}$$

where WE_a is the *WE* signal after the preparation steps from Sect. 2.3.1, *T* is the temperature in °C, and α, β_z (z = 0, 1, 2, 3) are

250   the determined regression parameters. We give a more detailed description of how to obtain Eq. (3) and (4) in the supplement and show the regression parameters in Table S3. To calculate the amount fractions, $WE_{NO,c}$ and $WE_{NO2,c}$ are then divided by the corresponding sensitivities of the sensors (Table S1). In the following sections we will often use NO_x (NO + NO_2). For the ECS, this means

$$x_{NO_x}(t) = \frac{WE_{NO,c}(t)}{S_{NO}} + \frac{WE_{NO_2,c}(t)}{S_{NO_2}}, \tag{5}$$

255   in which the summands are moving averages as described in Sect. 2.3.3 to consider the response time of the ECSs.

3.2 Validation of ECSs performance

3.2.1 Intercomparison of ECS setups
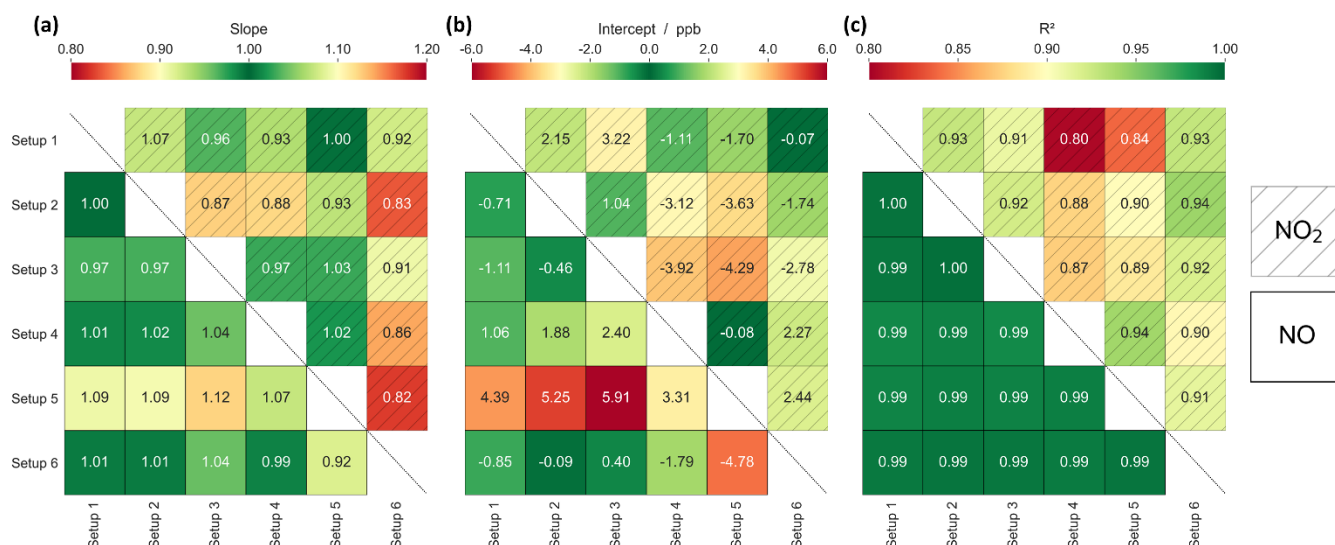
Figure 4: From left to right: (a) slopes, (b) intercepts, and (c) R² of the linear regressions between one setup and any other setup for ≈ 286 hours of measurements (≈ 75 hours in-flight). The lower triangle, depicted with black framed rectangles are the NO sensors results. The grey diagonally striped rectangles in the upper triangle show the results of the NO₂ sensors. The red to green color map indicates the range from worst to best values, respectively.

Figure 4 shows the intercomparison of all ECS setups after applying the corrections presented in Sect. 3.1, by performing linear regression analysis including their slopes, the intercepts, and coefficients of determination R^2. All NO sensors are in good agreement with slopes ranging from 0.92 to 1.12, intercepts from ±0.09 ppb to ±5.91 ppb and $R^2 > 0.99$, whereas for NO_2 slopes range from 0.82 to 1.07, intercepts from ±0.07 ppb to ±4.29 ppb, and R^2 from 0.80 to 0.94. Although the R^2 is high for all setups, the regressions of setups #4 and #5 with the NO sensors show greater variability in terms of intercepts and slopes. For NO, setup #5 has the highest offset of 5.91 ppb and a larger slope compared to all other setups. For NO_2 the results are not as definite but the R^2 is generally lower for setups #4 and #5, indicating higher noise of the sensors. This is also further supported by Fig. S8 with the noise of the sensor setups #4 and #5 at 5.03 ppb and 3.59 ppb for NO, and 6.32 ppb and 5.43 ppb for NO_2, respectively. Setups #3 and #6 have similar precisions for NO compared to setup #2 with values of 1.45 ppb and 1.98 ppb compared to 1.95 ppb, respectively; however, their noise for NO_2 is approximately 55 % and 61 % higher than for setup #2. Therefore, we exclusively use setup #2 in the following given the consistent agreement to other sensors, the lower noise, and the high in-flight data coverage > 98 %.

The regression parameters for NO_2 are more variable than for NO. One possible reason is the smaller temperature dependence for NO_2. As a result, *AUX*, for example for setup #2, varies only between 220 to 240 mV, whereas NO varies between 300 to 400 mV (Fig. 3 and S6). This indicates that the temperature influence is the dominant contribution for the baseline correction of the NO sensor, whereas the *WE* of the NO_2 sensor could additionally be influenced by other interfering factors that do not

280 affect the *AUX* and are not accounted for here. Another factor is the much larger number of data points for NO (n = 4026) than for NO$_2$ (n = 155) for amount fractions above 50 ppb, leading to a more stable regression line for NO.

3.2.2 Noise reduction
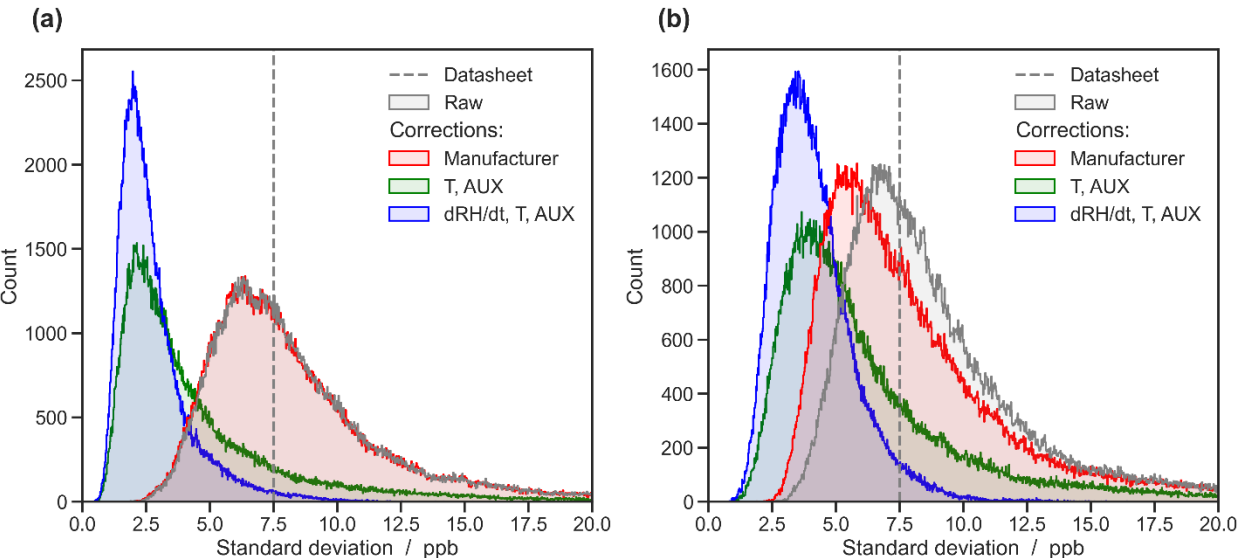
Figure 5: Distributions of standard deviations calculated inside 31 s windows shown for (a) NO and (b) NO$_2$ sensors of setup #2
285 **filtered for flights above 100 m to avoid engine exhaust peaks (number of data points = 270 198). Adding d*RH*/d*t* to the correction procedure leads to a narrower distribution by reducing high changes of the signal on a short timescale.**

Figure 5 shows the distributions of the standard deviations of the NO (a) and NO$_2$ (b) sensors for each 31 s windows which were used to calculate the moving average (Sect. 2.3.3). The data were filtered for periods with height above 100 m (n = 270 198) to avoid engine exhaust peaks that would result in high standard deviations because of the high changes in
290 concentrations inside these time windows. The correction used here, shown in blue and green, results in the lowest noise with modal values for NO of 2.03 ppb for the correction with *T* and *AUX*, and 1.95 ppb when d*RH*/d*t* is additionally included in the correction, whereas for NO$_2$, the noise modal values are 3.66 ppb and 3.32 ppb. Besides the change in peak position, the distributions become narrower when correcting with d*RH*/d*t*. This leads to significantly higher peaks of around 60 % for both analytes because the number of data points with standard deviations above 3 ppb for NO and above 5 ppb for NO$_2$ decreases,
295 highlighting the significant noise reduction when including d*RH*/d*t* in the correction procedure.

3.2.3 Comparison of ECSs with the MIRO MGA
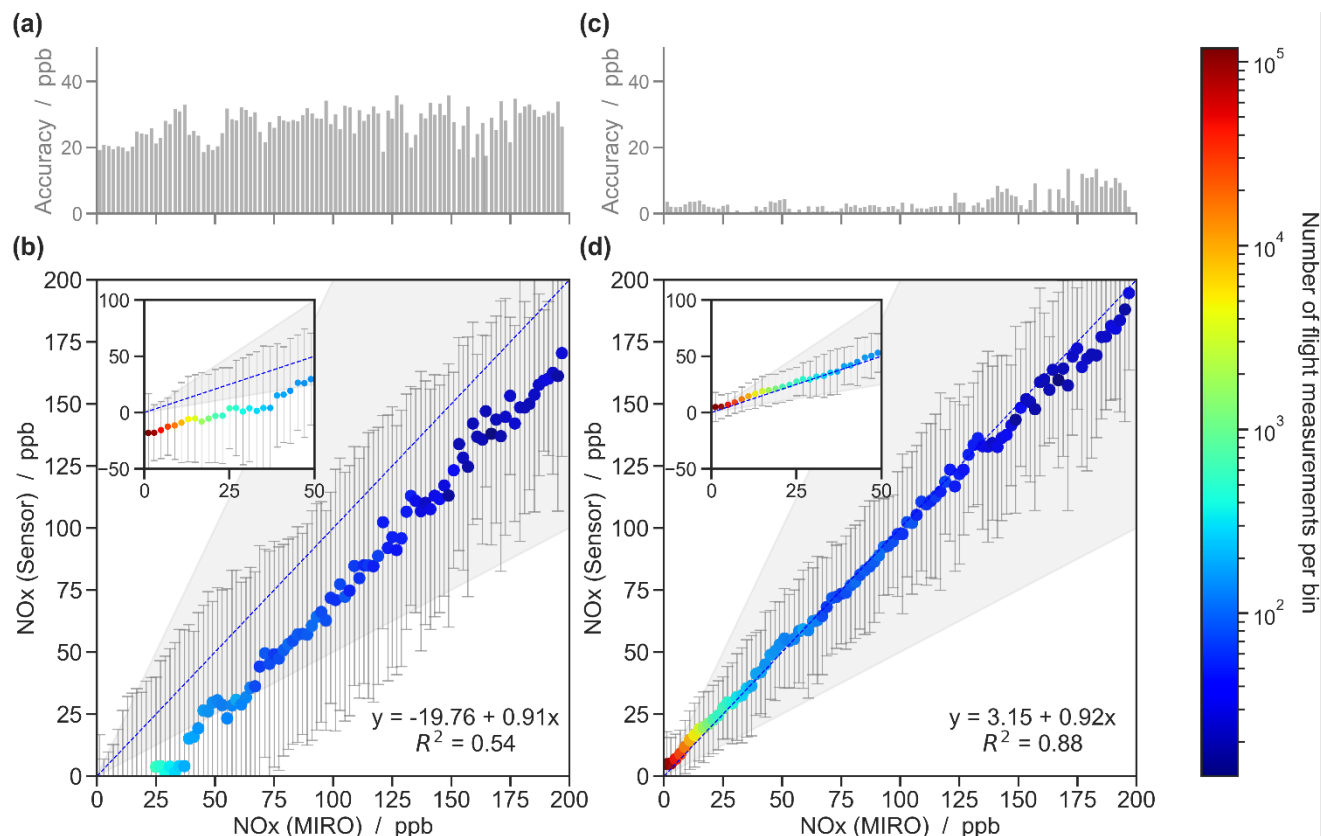
Figure 6: Scatterplots of the in-flight (≈ 75 hours) corrected NO_x sensor data (setup #2) vs. MIRO MGA data (reference) classified in 2 ppb bins and two times the standard deviations (± 2σ). Shown in (a) and (c), are the accuracies for each bin, i.e., the absolute
300   **difference between sensor and MIRO MGA data per bin. Plots (a) and (b) represent the corrections as recommended by the manufacturer, whereas (c) and (d), provide the results of our correction method. The dashed blue line marks the 1:1 line and the range of 2:1 and 1:2 is shaded in grey. The inlet plots show the data in a higher resolution from 0 to 50 ppb of the reference instrument. In addition, the linear regression results are shown on the bottom right**

Figure 6 (a) and (b) show the amount fractions of NO_x for sensor setup #2 (master setup, see section 2.3.1) following the

305   corrections recommended by the manufacturer as described in Sect. 2.3.3 whereas Figure 6 (c) and (d) show the correction

method developed in this work compared to the MIRO MGA used as a reference device. Additionally, comparisons of all

setups with the MIRO MGA are shown in Figure S10. As shown in Fig. 6 (a) and (c) the deviations of the sensor values to

MIRO decreased from an absolute average of 27.3 ± 4.8 ppb to 3.5 ± 3.1 ppb. This means an absolute accuracy improvement

by nearly an order of magnitude. The accuracy increase is mainly the result of the improved offsets changing

310   from -13.15 ppb, -8.29 ppb, and -19.76 ppb to 9.12 ppb, -6.76 ppb, and 3.15 ppb for NO, NO_2 (Fig. S9), and NO_x, respectively.

Precision also improved, reflected by the decrease of the associated error bars in Fig. 6 resulting in a higher coefficient of

determination from 0.54 to 0.88. In general, NO and NO_2 measurements corrected with our method, and the resulting NO_x

values are close to the 1:1 line. Moreover, the two standard deviations corresponding to 95 % of the data in each bin, are within a factor of 2 above 20 ppb, which is particularly driven by the dRH/dt correction, as also shown in Fig. 5.

315 While on average there is agreement within 3.5 ppb for NO_x between the MIRO and ECSs at both high and low concentrations this agreement is not evident for the lower amount fractions of NO or NO_2 (Fig. S9). For NO an average overestimation of 34.4 % is observed below 40 ppb, that increases to an average deviation of up to 600 % in the range of 0 to 5 ppb, whereas for NO_2 an underestimation of 31.3 % is observed for amount fractions below 25 ppb, increasing to 300 % below 5 ppb, because of the small absolute numbers. It is possible that the 8 m sampling line to the MIRO could influence the composition of NO

320 and NO_2 as an in-line reaction of NO with O_3 could lead to higher NO_2 and lower NO concentrations, compared to the sensors that have no sampling line. However, this effect is expected to be minor due to the short sample residence time of 5 s. In addition, other parameters may influence the performance of the electrochemical sensors compared to the MIRO, such as cross sensitivities to other gases, the wind speed (Mead et al., 2013) or the atmospheric pressure. In this study, measurements of gases are limited to CO, CO_2, CH_4, N_2O, H_2O, and O_3 performed by the MIRO MGA (Tillmann et al., 2022). No significant

325 cross interference was observed under the present atmospheric concentrations, as shown in Fig. S12. To quantify possible influences from wind speed and atmospheric pressure, a measuring chamber of a constant volumetric flow together with pressure sensors will be used in future campaigns.

Besides the above direct influences, there is also the possibility of sensor drifts, i.e., a change of the sensor signal with time. Wei et al. (2018) estimated a possible drift of < 2 ppb/month whereas Mead et al. (2013) state that the sensitivity of the sensors

330 remained unchanged over an 11-month measurement period. For our deployment duration of 1.5 months, sensor drifts are therefore expected to be within the uncertainty of the measurements which is also reflected by the good agreement of the ECS and the MIRO in Fig. 6 and S10. Furthermore, Fig. S11 shows the timeseries of all sensors during different flight days in May and June to evaluate the influence of such sensor drifts. The consistent correlation of all setups to the MIRO highlights the stability of the sensors during this study. However, we promote the need for controlled laboratory measurements in the future

335 to evaluate long-term influences on the stability of the ECS signals including sensor drifts.

Evidently, with the manufacturer's correction, amount fractions (Fig. 6 (a)) cannot be accurately quantified predominantly due to the high offset of -19.76 ppb. One possible reason is that in Eq. (1) and (2) the same temperature compensation factors are used for all sensors, whereas each sensor may react differently to a temperature change, which is also shown by our regression parameters in Table S3. Another cause could be a drift of the zero value, which is not caught by the temperature and AUX

340 correction in these equations. In our method, sensor drifts are corrected by using minimum values of measured WE voltages following the procedure described in Mead et al. (2013) as discussed in Sect. 2.3 and the supplement.

3.3 Detection of anthropogenic NO$_x$ emission sources
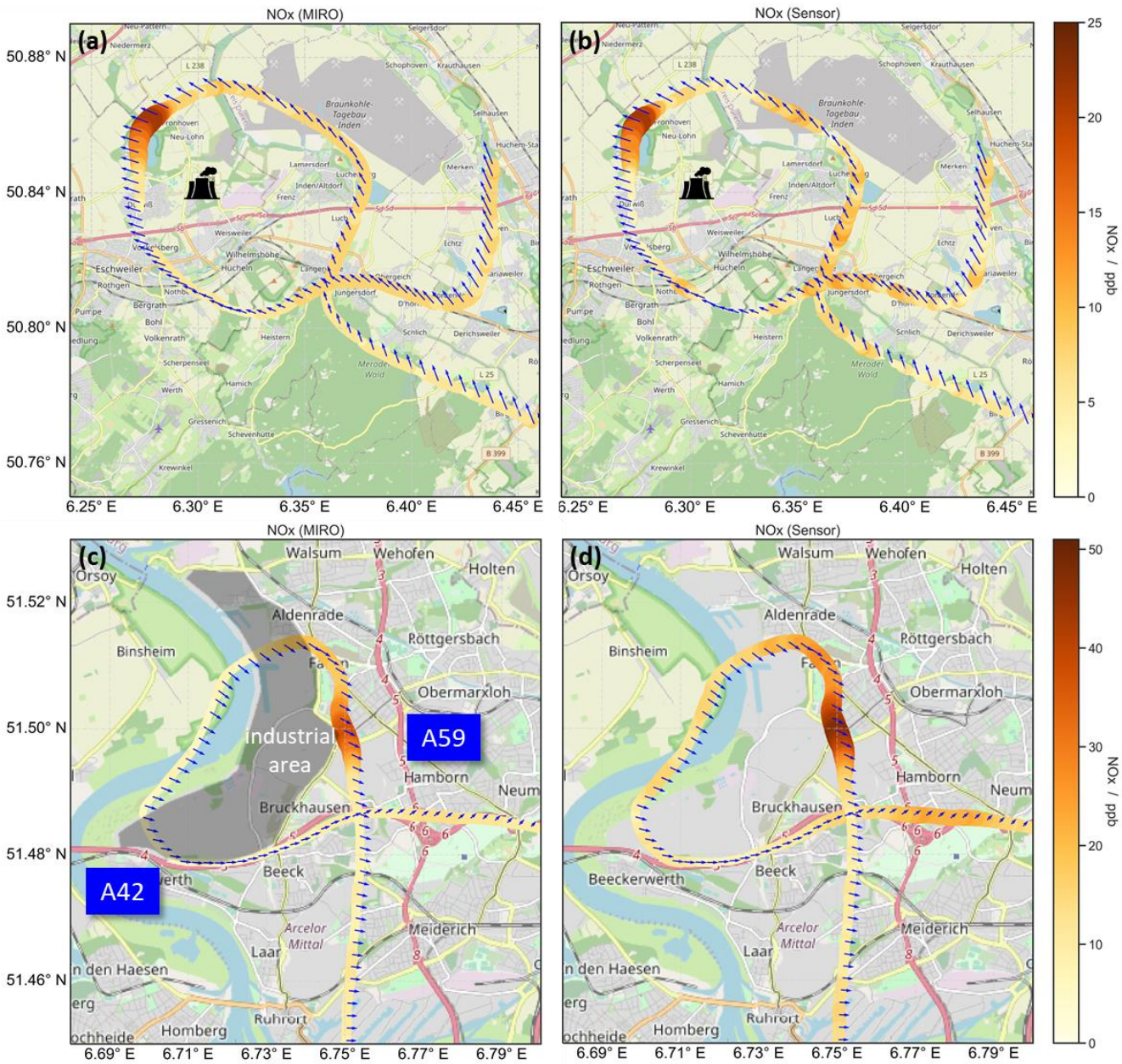
Figure 7: Amount fractions of NOx are shown by color and size for the MIRO MGA (a, c) and the corrected sensor data of setup #2 (b, d) during flights in North Rhine-Westphalia, Germany, near and in the cities of Eschweiler and Duisburg, respectively (© OpenStreetMap contributors 2022. Distributed under the Open Data Commons Open Database License (ODbL) v1.0). The arrows orientation and length indicate the wind direction and wind speed (2.1 to 7.2 m s^{-1} for (a, b) and 1.0 to 2.6 m s^{-1} for (c, d); data from EURAD-IM, WRF), respectively. With this, the emission sources can be narrowed down to a lignite-fired power plant located southeast of the detected peak (a, b) and to a steel industry (c, d), located in the grey shaded area.

After the successful validity check by comparing the corrected sensor data with the reference device in the former section, we now present possible applications and the potential of ECS for airborne measurements. Figure 7 (a) and (b) show the flight path on 06 May 2020 between 07:30 and 08:30 UTC in Eschweiler, North Rhine-Westphalia, Germany when using the reference instrument and the ECS sensors, respectively. Another example is shown in Fig. 7 (c) and (d) during a Zeppelin

355 flight over Duisburg Nord (Hamborn), North Rhine-Westphalia, Germany on 07 May 2020 between 13:30 and 14:15 UTC. As depicted in Fig. 7 (a) NO_x background concentrations are 4.9 ± 2.0 ppb and increase significantly in the northwest to a maximum of 21.3 ± 2.2 ppb due to the emissions from the lignite-fired power plant located near the flight path (Tillmann et al., 2022), further supported by the wind data that were extracted from high-resolution model simulations. When applying the correction method recommended by the manufacturer for the ECSs (Sect. 2.3.3), background concentrations of NO_x are at -

360 8.6 ± 5.2 ppb and the industrial plume emissions at 11.3 ± 17.3 ppb highlighting the limitations of this method. However, after applying the correction method developed in this work, shown in Fig. 7 (b), a significant improvement is observed with background concentrations at 3.5 ± 4.2 ppb and the power plant plume average at 21.4 ± 6.6 ppb (Fig. S13 (a)). This results in 40 % higher background concentrations for the sensor measurements in comparison to the MIRO and 5 % lower concentrations for the in-plume measurements.

365 Similar results can be seen in Fig. (c) and (d); Duisburg is known for its industry – there is a steel mill in this district, which is supplied with electricity by the gas-fired combined heat and power plant located on the site. In addition, the motorways A42 and A59 run through the area. Westerly winds indicate that the source of emissions during the observed maximum amount fractions of 37.7 ± 6.1 ppb for the MIRO and 47.1 ± 6.4 ppb (Fig. S13 (b)) for the sensor measurements, are from the steel mill and the heat power plant. The influence of highway emissions on the NO_x concentrations is observed at around 51.48° N

370 and 6.77° E when Southerly wind directions transported emissions from the A42 and A59 highways to our sampling line. This is especially evident for the sensor data (d) but also observable for the MIRO (c). Here, the peak values are 13.8 ± 0.7 ppb and 22.6 ± 3.6 ppb for the MIRO and the ECS, respectively.

These case examples, highlight the potential of the ECS to detect emission sources with concentrations down to 20 ppb. Although, there are larger relative uncertainties due to the deviations of the individual NO and NO_2 sensors (see Sect. 3) the

375 ECSs show better agreement with the MIRO at higher concentrations, especially for NO_x further promoting their potential for airborne applications.

4 Conclusions

We showed that electrochemical sensors (ECS) can be successfully used for airborne in situ measurements in the PBL. For this, we used a Zeppelin NT to perform an in-flight comparison of six sensor setups with a reference device during two

380 measurement campaigns, including targeted and commercial flights, in Germany from April to June 2020. Each setup consisted of four electrochemical sensors for CO, NO, NO_2, and Ox ($NO_2 + O_3$) and one sensor for temperature and relative humidity.

These were installed in a custom-built hatch box mounted under the gondola. A quantum cascade laser-based multi-compound gas analyzer, called MIRO MGA, was placed as a reference instrument inside the gondola with an inlet line beside the ECSs.

We developed a stand-alone correction method, i.e., independent of a reference device, for the ECSs that accounts for external influences on the NO and NO_2 sensor signals by using the variability of the auxiliary electrode voltage, temperature, and the relative humidity gradient. We show that this correction method substantially improves the accuracy down to 6.3 ± 5.7 ppb and 8.7 ± 5.9 ppb and lowers the noise (1 σ) of the ECS to 1.92 ppb and 3.32 ppb for NO and NO_2, respectively. The combination of both sensor types (NO and NO_2) leads to a further improved accuracy of 3.5 ± 3.1 ppb for NO_x. When compared to the MIRO MGA good agreement with a coefficient of determination of 0.88 and a slope of 0.92 is achieved for NO_x measurements. However, at lower concentrations below 40 ppb and 25 ppb average deviations of 34.4 % and -31.3 % for NO and NO_2, respectively, were evident. Below 5 ppb, these deviations increased up to 300 % and -600 %, because of the small absolute values, indicating the limitations of ECSs for accurate quantification at lower amount fractions.

We highlight the potential to use the sensors for emission source identification during the Zeppelin flights by identifying emissions from a lignite-fired power plant with a peak of approximately 21 ppb of NO_x and from a large industrial area in Duisburg with a peak above 40 ppb.

Results from this work emphasize the potential of these sensors for in situ airborne applications and provide a first milestone for future quality-assured use onboard UAVs without the need of a reference device. A comprehensive characterization in the laboratory, including the simulation of airborne conditions, before and after such applications, will improve the ECS data quality even further.

Data availability. The data are available at https://doi.org/10.26165/JUELICH-DATA/6D8B70 (Schuldt et al., 2022).

Author contribution. RT, FR, and AKS designed the experiments and flight campaigns. BW, CW, and FR carried them out. GIG and TS visualized the data. AKS, TAJK, GIG, RT, and TS contributed to the interpretation of the results. GIG and TS prepared the manuscript with contributions from all co-authors.

Acknowledgments. We acknowledge the support of Deutsche Zeppelin Reederei (DZR) and Zeppelin Luftschifftechnik GmbH (ZLT). We would like to thank Anne Caroline Lange, Elmar Friese and Philipp Franke for the high-resolution Weather Research and Forecasting Model (WRF) and EURopean Air pollution Dispersion-Inverse Model (EURAD-IM) simulations, Achim Grasse for the laboratory measurements, and Morten Hundt and Oleg Aseev for instrumentation support of the MIRO MGA. The authors gratefully acknowledge the computing time granted through JARA on the supercomputer JURECA at Forschungszentrum Jülich.

The authors declare that they have no conflict of interest.

References

Alphasense: AAN 103 Shielding Toxic Sensors from Electromagnetic Interference, 2013.

Alphasense: Datasheet: NO2-B43F Nitrogen Dioxide Sensor 4-Electrode, 2019a.

Alphasense: Datasheet: NO-B4 Nitric Oxide Sensor 4-Electrode, 2019b.

Alphasense: AAN 803-05 Correcting for background currents in four electrode toxic gas sensors, 2019c.

Alphasense: Datasheet: OX-B431 Oxidising Gas Sensor 4-Electrode; Ozone + Nitrogen Dioxide, 2019d.

Alphasense: Datasheet: CO-B4 Carbon Monoxide Sensor 4-Electrode, 2019e.

Alphasense: Datasheet: Individual Sensor Board (ISB) Alphasense B4 4-Electrode Gas Sensors, 2019f.

Apte, J. S., Messier, K. P., Gani, S., Brauer, M., Kirchstetter, T. W., Lunden, M. M., Marshall, J. D., Portier, C. J., Vermeulen, R. C. H., and Hamburg, S. P.: High-Resolution Air Pollution Mapping with Google Street View Cars: Exploiting Big Data, Environmental Science & Technology, 51, 6999-7008, 10.1021/acs.est.7b00891, 2017.

Baron, R. and Saffell, J.: Amperometric Gas Sensors as a Low Cost Emerging Technology Platform for Air Quality Monitoring Applications: A Review, ACS Sens, 2, 1553-1566, 10.1021/acssensors.7b00620, 2017.

Bretschneider, L., Schlerf, A., Baum, A., Bohlius, H., Buchholz, M., Düsing, S., Ebert, V., Erraji, H., Frost, P., Käthner, R., Krüger, T., Lange, A. C., Langner, M., Nowak, A., Pätzold, F., Rüdiger, J., Saturno, J., Scholz, H., Schuldt, T., Seldschopf, R., Sobotta, A., Tillmann, R., Wehner, B., Wesolek, C., Wolf, K., and Lampert, A.: MesSBAR—Multicopter and Instrumentation for Air Quality Research, Atmosphere, 13, 629, 10.3390/atmos13040629, 2022.

Bytnerowicz, A., Omasa, K., and Paoletti, E.: Integrated effects of air pollution and climate change on forests: A northern hemisphere perspective, Environmental Pollution, 147, 438-445, 10.1016/j.envpol.2006.08.028, 2007.

Chen, J. and Hoek, G.: Long-term exposure to PM and all-cause and cause-specific mortality: A systematic review and meta-analysis, Environment International, 143, 105974, 10.1016/j.envint.2020.105974, 2020.

Cross, E. S., Williams, L. R., Lewis, D. K., Magoon, G. R., Onasch, T. B., Kaminsky, M. L., Worsnop, D. R., and Jayne, J. T.: Use of electrochemical sensors for measurement of air pollution: correcting interference response and validating measurements, Atmospheric Measurement Techniques, 10, 3575-3588, 10.5194/amt-10-3575-2017, 2017.

Dallo, F., Zannoni, D., Gabrieli, J., Cristofanelli, P., Calzolari, F., de Blasi, F., Spolaor, A., Battistel, D., Lodi, R., Cairns, W. R. L., Fjæraa, A. M., Bonasoni, P., and Barbante, C.: Calibration and assessment of electrochemical low-cost sensors in remote alpine harsh environments, Atmospheric Measurement Techniques, 14, 6005-6021, 10.5194/amt-14-6005-2021, 2021.

Gu, Q., D, R. M., and Jia, C.: Developing a Modular Unmanned Aerial Vehicle (UAV) Platform for Air Pollution Profiling, Sensors (Basel), 18, 4363, 10.3390/s18124363, 2018.

Han, P., Mei, H., Liu, D., Zeng, N., Tang, X., Wang, Y., and Pan, Y.: Calibrations of Low-Cost Air Pollution Monitoring Sensors for CO, NO2, O3, and SO2, Sensors (Basel), 21, 256, 10.3390/s21010256, 2021.

Hossain, M., Saffell, J., and Baron, R.: Differentiating NO2 and O3 at Low Cost Air Quality Amperometric Gas Sensors, ACS Sensors, 1, 1291-1294, 10.1021/acssensors.6b00603, 2016.

Huangfu, P. and Atkinson, R.: Long-term exposure to NO2 and O3 and all-cause and respiratory mortality: A systematic review and meta-analysis, Environment International, 144, 105998, 10.1016/j.envint.2020.105998, 2020.

450 Hundt, P. M., Tuzson, B., Aseev, O., Liu, C., Scheidegger, P., Looser, H., Kapsalidis, F., Shahmohammadi, M., Faist, J., and Emmenegger, L.: Multi-species trace gas sensing with dual-wavelength QCLs, Applied Physics B, 124, 108, 10.1007/s00340-018-6977-y, 2018.

IPCC, Masson-Delmotte, V. Z., P.; Pirani, A.; Connors, S.L.; Péan, C.; Berger, S.; Caud, N.; Chen, Y.; Goldfarb, L.; Gomis, M.I.; Huang, M.; Leitzell, K.; Lonnoy, E.; Matthews, J.B.R.; Maycock, T.K.; Waterfield, T.; Yelekçi, O.; Yu, R.; Zhou, B.

455 (Ed.): Climate Change 2021: The Physical Science Basis. Contribution of Working Group I to the Sixth Assessment Report of the Intergovernmental Panel on Climate Change, Cambridge University Press, Cambridge, United Kingdom and New York, NY, USA, In press, 10.1017/9781009157896, 2021.

Kampa, M. and Castanas, E.: Human health effects of air pollution, Environ Pollut, 151, 362-367, 10.1016/j.envpol.2007.06.012, 2008.

460 Lewis, A. C., Lee, J. D., Edwards, P. M., Shaw, M. D., Evans, M. J., Moller, S. J., Smith, K. R., Buckley, J. W., Ellis, M., Gillot, S. R., and White, A.: Evaluating the performance of low cost chemical sensors for air pollution research, Faraday Discuss, 189, 85-103, 10.1039/c5fd00201j, 2016.

Liu, C., Tuzson, B., Scheidegger, P., Looser, H., Bereiter, B., Graf, M., Hundt, M., Aseev, O., Maas, D., and Emmenegger, L.: Laser driving and data processing concept for mobile trace gas sensing: Design and implementation, Review of Scientific

465 Instruments, 89, 065107, 10.1063/1.5026546, 2018.

Mawrence, R., Munniks, S., and Valente, J.: Calibration of Electrochemical Sensors for Nitrogen Dioxide Gas Detection Using Unmanned Aerial Vehicles, Sensors (Basel), 20, 7332, 10.3390/s20247332, 2020.

Mclaughlin, S. B.: Effects of Air Pollution on Forests - a Critical Review, Japca J Air Waste Ma, 35, 512-534, Doi 10.1080/00022470.1985.10465928, 1985.

470 Mead, M. I., Popoola, O. A. M., Stewart, G. B., Landshoff, P., Calleja, M., Hayes, M., Baldovi, J. J., McLeod, M. W., Hodgson, T. F., Dicks, J., Lewis, A., Cohen, J., Baron, R., Saffell, J. R., and Jones, R. L.: The use of electrochemical sensors for monitoring urban air quality in low-cost, high-density networks, Atmospheric Environment, 70, 186-203, 10.1016/j.atmosenv.2012.11.060, 2013.

Messier, K. P., Chambliss, S. E., Gani, S., Alvarez, R., Brauer, M., Choi, J. J., Hamburg, S. P., Kerckhoffs, J., Lafranchi, B.,

475 Lunden, M. M., Marshall, J. D., Portier, C. J., Roy, A., Szpiro, A. A., Vermeulen, R. C. H., and Apte, J. S.: Mapping Air Pollution with Google Street View Cars: Efficient Approaches with Mobile Monitoring and Land Use Regression, Environmental Science & Technology, 52, 12563-12572, 10.1021/acs.est.8b03395, 2018.

Mijling, B., Jiang, Q., de Jonge, D., and Bocconi, S.: Field calibration of electrochemical NO2 sensors in a citizen science context, Atmospheric Measurement Techniques, 11, 1297-1312, 10.5194/amt-11-1297-2018, 2018.

480 Mueller, M., Meyer, J., and Hueglin, C.: Design of an ozone and nitrogen dioxide sensor unit and its long-term operation within a sensor network in the city of Zurich, Atmospheric Measurement Techniques, 10, 3783-3799, 10.5194/amt-10-3783-2017, 2017.

Orellano, P., Reynoso, J., Quaranta, N., Bardach, A., and Ciapponi, A.: Short-term exposure to particulate matter (PM10 and PM2.5), nitrogen dioxide (NO2), and ozone (O3) and all-cause and cause-specific mortality: Systematic review and meta-

485 analysis, Environment International, 142, 105876, 10.1016/j.envint.2020.105876, 2020.

Pang, X., Shaw, M. D., Gillot, S., and Lewis, A. C.: The impacts of water vapour and co-pollutants on the performance of electrochemical gas sensors used for air quality monitoring, Sensors and Actuators B: Chemical, 266, 674-684, 10.1016/j.snb.2018.03.144, 2018.

Pang, X., Chen, L., Shi, K., Wu, F., Chen, J., Fang, S., Wang, J., and Xu, M.: A lightweight low-cost and multipollutant sensor

490 package for aerial observations of air pollutants in atmospheric boundary layer, Sci Total Environ, 764, 142828, 10.1016/j.scitotenv.2020.142828, 2021.

Pang, X. B., Shaw, M. D., Lewis, A. C., Carpenter, L. J., and Batchellier, T.: Electrochemical ozone sensors: A miniaturised alternative for ozone measurements in laboratory experiments and air-quality monitoring, Sensor Actuat B-Chem, 240, 829-837, 10.1016/j.snb.2016.09.020, 2017.

495 Pochwala, S., Gardecki, A., Lewandowski, P., Somogyi, V., and Anweiler, S.: Developing of Low-Cost Air Pollution Sensor-Measurements with the Unmanned Aerial Vehicles in Poland, Sensors (Basel), 20, 3582, 10.3390/s20123582, 2020.

Popoola, O. A. M., Stewart, G. B., Mead, M. I., and Jones, R. L.: Development of a baseline-temperature correction methodology for electrochemical sensors and its implications for long-term stability, Atmospheric Environment, 147, 330-343, 10.1016/j.atmosenv.2016.10.024, 2016.

500 Popoola, O. A. M., Carruthers, D., Lad, C., Bright, V. B., Mead, M. I., Stettler, M. E. J., Saffell, J. R., and Jones, R. L.: Use of networks of low cost air quality sensors to quantify air quality in urban settings, Atmospheric Environment, 194, 58-70, 10.1016/j.atmosenv.2018.09.030, 2018.

Quah, E. and Boon, T. L.: The economic cost of particulate air pollution on health in Singapore, Journal of Asian Economics, 14, 73-90, 10.1016/S1049-0078(02)00240-3, 2003.

505 Rai, A. C., Kumar, P., Pilla, F., Skouloudis, A. N., Di Sabatino, S., Ratti, C., Yasar, A., and Rickerby, D.: End-user perspective of low-cost sensors for outdoor air pollution monitoring, Sci Total Environ, 607-608, 691-705, 10.1016/j.scitotenv.2017.06.266, 2017.

Sahu, R., Nagal, A., Dixit, K. K., Unnibhavi, H., Mantravadi, S., Nair, S., Simmhan, Y., Mishra, B., Zele, R., Sutaria, R., Motghare, V. M., Kar, P., and Tripathi, S. N.: Robust statistical calibration and characterization of portable low-cost air quality

510 monitoring sensors to quantify real-time O3 and NO2 concentrations in diverse environments, Atmospheric Measurement Techniques, 14, 37-52, 10.5194/amt-14-37-2021, 2021.

Samad, A., Obando Nunez, D. R., Solis Castillo, G. C., Laquai, B., and Vogt, U.: Effect of Relative Humidity and Air Temperature on the Results Obtained from Low-Cost Gas Sensors for Ambient Air Quality Measurements, Sensors (Basel), 20, 5175, 10.3390/s20185175, 2020.

515 Savitzky, A. and Golay, M. J. E.: Smoothing and Differentiation of Data by Simplified Least Squares Procedures, Analytical Chemistry, 36, 1627-1639, 10.1021/ac60214a047, 1964.

Schuldt, T., Georgios, I. G., Christian, W., Franz, R., Benjamin, W., Thomas, A. J. K., Astrid, K.-S., and Ralf, T.: Replication Data for: Zeppelin flights 2020: Electrochemical sensors (V1), Jülich DATA [dataset], 10.26165/JUELICH-DATA/6D8B70, 2022.

520 Schuyler, T. and Guzman, M.: Unmanned Aerial Systems for Monitoring Trace Tropospheric Gases, Atmosphere, 8, 206, 10.3390/atmos8100206, 2017.

Shusterman, A. A., Teige, V. E., Turner, A. J., Newman, C., Kim, J., and Cohen, R. C.: The BErkeley Atmospheric CO2 Observation Network: initial evaluation, Atmos Chem Phys, 16, 13449-13463, 10.5194/acp-16-13449-2016, 2016.

Spinelle, L., Gerboles, M., Villani, M. G., Aleixandre, M., and Bonavitacola, F.: Field calibration of a cluster of low-cost

525 available sensors for air quality monitoring. Part A: Ozone and nitrogen dioxide, Sensors and Actuators B: Chemical, 215, 249-257, 10.1016/j.snb.2015.03.031, 2015.

Spinelle, L., Gerboles, M., Villani, M. G., Aleixandre, M., and Bonavitacola, F.: Field calibration of a cluster of low-cost commercially available sensors for air quality monitoring. Part B: NO, CO and CO2, Sensors and Actuators B: Chemical, 238, 706-715, 10.1016/j.snb.2016.07.036, 2017.

530 Stetter, J. R. and Li, J.: Amperometric gas sensors: a review, Chem Rev, 108, 352-366, 10.1021/cr0681039, 2008.

Sun, L., Wong, K. C., Wei, P., Ye, S., Huang, H., Yang, F., Westerdahl, D., Louie, P. K., Luk, C. W., and Ning, Z.: Development and Application of a Next Generation Air Sensor Network for the Hong Kong Marathon 2015 Air Quality Monitoring, Sensors (Basel), 16, 211, 10.3390/s16020211, 2016.

Tillmann, R., Gkatzelis, G. I., Rohrer, F., Winter, B., Wesolek, C., Schuldt, T., Lange, A. C., Franke, P., Friese, E., Decker,

535 M., Wegener, R., Hundt, M., Aseev, O., and Kiendler-Scharr, A.: Air quality observations onboard commercial and targeted Zeppelin flights in Germany – a platform for high-resolution trace-gas and aerosol measurements within the planetary boundary layer, Atmos. Meas. Tech., 15, 3827-3842, 10.5194/amt-15-3827-2022, 2022.

Villa, T. F., Salimi, F., Morton, K., Morawska, L., and Gonzalez, F.: Development and Validation of a UAV Based System for Air Pollution Measurements, Sensors (Basel), 16, 2202, 10.3390/s16122202, 2016.

540 Von Schneidemesser, E., Driscoll, C., Rieder, H. E., and Schiferl, L. D.: How will air quality effects on human health, crops and ecosystems change in the future?, Philosophical Transactions of the Royal Society A: Mathematical, Physical and Engineering Sciences, 378, 20190330, 10.1098/rsta.2019.0330, 2020.

Wei, P., Ning, Z., Ye, S., Sun, L., Yang, F., Wong, K. C., Westerdahl, D., and Louie, P. K. K.: Impact Analysis of Temperature and Humidity Conditions on Electrochemical Sensor Response in Ambient Air Quality Monitoring, Sensors (Basel), 18, 59,

545 10.3390/s18020059, 2018.

WHO: WHO global air quality guidelines: particulate matter (PM2.5 and PM10, ozone, nitrogen dioxide, sulfur dioxide and carbon monoxide), World Health Organization, 978-92-4-003422-8, 2021.

WMO, Lewis, A. C., von Schneidemesser, E., and Peltier, R. E. (Eds.): Low-cost sensors for the measurement of atmospheric composition: overview of topic and future applications, World Meteorological Organization (WMO), Geneva, 978-92-63-

550   11215-6, 2018.

Zimmerman, N., Presto, A. A., Kumar, S. P. N., Gu, J., Hauryliuk, A., Robinson, E. S., and Robinson, A. L.: A machine learning calibration model using random forests to improve sensor performance for lower-cost air quality monitoring, Atmospheric Measurement Techniques, 11, 291-313, 10.5194/amt-11-291-2018, 2018.